

Millimeter-Wave Dielectric Properties of Highly Refractive Single Crystals Characterized by Waveguide Cavity Resonance

Ross T. Schermer¹, *Member, IEEE*, and Todd H. Stievater

Abstract—This paper reports precision measurements of the electromagnetic permittivity of five highly refractive, single-crystal materials, SrTiO₃, KTaO₃, rutile TiO₂, LiTaO₃, and LiNbO₃, using a single, well-controlled, frequency-scalable procedure over the frequency ranges 25–110 and 140–220 GHz. Real permittivity values were highly consistent for different samples measured across multiple frequency bands. For SrTiO₃, KTaO₃, and TiO₂, real permittivities were more consistent with lower frequency values than typically reported in the millimeter-wave region of the spectrum. Real permittivities of LiTaO₃ and LiNbO₃ agreed with most reported data. The intrinsic dielectric loss of SrTiO₃, KTaO₃, and the extraordinary axis of rutile TiO₂ was also characterized over the ranges 25–110 and 140–220 GHz, and intrinsic loss per unit frequency was found to be consistent with values measured at other frequencies by dielectric resonators and quasi-optical techniques.

Index Terms—Dielectric constant, dielectric losses, dielectric measurement, ferroelectric materials, high-*k* dielectric materials, millimeter-wave measurements, millimeter-wave technology.

I. INTRODUCTION

HIGHLY refractive materials with large permittivity have long been of interest for electronics operating in the millimeter-wave frequency range (30–300 GHz), and are integral to applications such as electro-optic modulators [1], [2], electronically tunable microwave devices [3]–[5], high-*Q* resonant cavities [6], [7], and high temperature superconductors [4], [8]. Among other things, the large permittivity facilitates component miniaturization [9], elevated capacitance [10], and wide tunability [11]–[13]. However, reported permittivities in the millimeter-wave region of the spectrum vary significantly [12]–[30], due to both the range and limitations of test methods employed, and the tendency for individual measurements to span only a limited frequency range.

This paper presents an experimental and theoretical investigation of five highly refractive, single-crystal materials, SrTiO₃, KTaO₃, rutile TiO₂, LiTaO₃, and LiNbO₃, using a single, well-controlled, frequency-scalable measurement procedure over the frequency ranges 25–110 and 140–220 GHz. This provides real permittivity values for each material and loss tangents for the higher loss materials that are both

consistent with a subset of reported values (particularly those measured at lower frequency), and highly consistent for samples measured across multiple frequency bands. For SrTiO₃, KTaO₃, and rutile TiO₂, in particular, the measured dielectric properties are more precise than previously reported over the millimeter-wave frequency range.

Measurements were based on a resonant cavity formed by a planar dielectric substrate placed between the flanges of two air-filled rectangular waveguides, as shown schematically in Fig. 1. This technique has been used previously to characterize various dielectrics [19], [27], [31]–[33], although a rigorous analysis of cavity response was not presented. In this paper, waveguide–flange cavities were used to measure the same dielectric sample over multiple millimeter-wave frequency bands. This was accomplished by simply interchanging the waveguides that form the cavity, which allowed consistent data to be collected for each dielectric sample over nearly a decade in frequency between 25 and 220 GHz. Measured cavity response was then compared to theory in order to extract the dielectric properties of the test samples. This analysis was necessary to account for both diffractive losses within the cavity and off-axis propagation, which cause measured cavity response to deviate from that of an ideal Fabry–Perot resonator.

Section II begins by describing the theoretical model for waveguide–flange cavity response. Experimental procedure and measurements of cavity response are presented in Section III for cavities based on single-crystal SrTiO₃, KTaO₃, rutile TiO₂, LiTaO₃, and LiNbO₃. Section IV then presents an analysis of dielectric properties based on comparison of cavity response with theory. Section V concludes by comparing the measured dielectric properties to literature values.

II. WAVEGUIDE–FLANGE CAVITY MODEL

The model for waveguide–flange cavity response used in this paper was that of a generalized Fabry–Perot resonator. In this model, the cavity transmission coefficient S_{21} and cavity reflection coefficient S_{11} are described by [34]

$$S_{21} \cong \frac{A\sqrt{B}\exp(-j\beta_{\text{eff}}L)}{1 - B\exp(-j2\beta_{\text{eff}}L)} \quad (1)$$

$$S_{11} \cong r' + \frac{AB\exp(-j2\beta_{\text{eff}}L)}{1 - B\exp(-j2\beta_{\text{eff}}L)} \quad (2)$$

where

$$A = \frac{t't}{r^2} \quad (3)$$

Manuscript received June 8, 2018; revised September 14, 2018; accepted October 29, 2018. Date of publication January 14, 2019; date of current version March 5, 2019. This work was supported by the U.S. Naval Research Laboratory. (*Corresponding author: Ross T. Schermer.*)

The authors are with the Optical Sciences Division, U.S. Naval Research Laboratory, Washington, DC 20375 USA (e-mail: ross.schermer@nrl.navy.mil).

Color versions of one or more of the figures in this paper are available online at <http://ieeexplore.ieee.org>.

Digital Object Identifier 10.1109/TMTT.2018.2883107

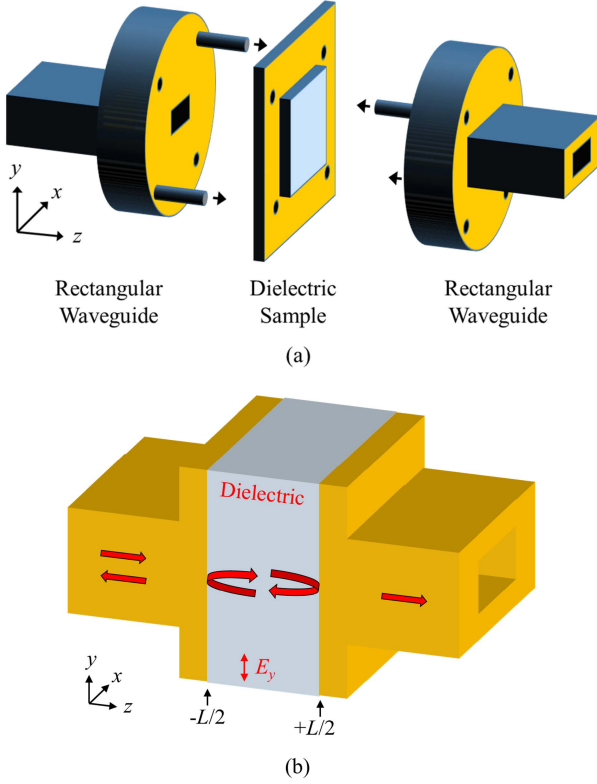


Fig. 1. (a) Schematic of rectangular waveguide, dielectric sample, and test fixture used for measurements over multiple waveguide frequency bands. (b) Cross section of a waveguide-flange cavity formed by two rectangular waveguides pressed against a planar dielectric. Red arrows: incident, reflected, and transmitted waveguide modes and resonant cavity mode. Flange field distributions are defined at $z = \pm L/2$. The electric field of the TE_{10} waveguide mode is parallel to the y -axis. The dielectric sample was held within a test fixture, with both faces extending beyond the surface of the fixture to ensure contact with each waveguide flange.

$$B = r^2 \exp(-2\alpha_{\text{eff}} L) \quad (4)$$

and β_{eff} is the phase propagation constant and α_{eff} the field attenuation coefficient of the resonant cavity mode. Parameters r' and t' are the reflection and transmission coefficients relating the incident TE_{10} waveguide mode to the reflected TE_{10} waveguide mode and the transmitted field distribution at the flange, respectively. Parameters r and t are the reflection and transmission coefficients relating the incident flange field distribution in the dielectric to the reflected flange field distribution and transmitted TE_{10} waveguide mode, respectively. In the preceding, the flange field distribution (discussed in Section IV) corresponds to the resonant cavity mode.

The effective refractive index n_{eff} and the effective loss tangent $\tan\delta_{\text{eff}}$ of the resonant cavity mode are related to β_{eff} , α_{eff} , and frequency f through expressions

$$n_{\text{eff}} = \frac{c\beta_{\text{eff}}}{2\pi f} \quad (5)$$

$$\tan\delta_{\text{eff}} \cong \frac{2\alpha_{\text{eff}}}{\beta_{\text{eff}}} = \frac{c\alpha_{\text{eff}}}{\pi f n_{\text{eff}}}. \quad (6)$$

It should be stressed that effective refractive index and effective loss tangent are properties of the cavity mode, rather than the dielectric within the cavity. Cavity response is related to the

TABLE I
SINGLE-CRYSTAL DIELECTRIC SUBSTRATES

Crystal	Orientation	Width (mm)	Thickness (μm)
SrTiO ₃	<100>	10x10	497, 995
KTaO ₃	<100>	5x5	519
Rutile TiO ₂	<100>	10x10	494, 1001
LiTaO ₃	X-Cut	10x10	495, 1005
LiNbO ₃	X-Cut	10x10	994

resonant frequency f_m and quality factor Q_m of the resonance through [35]

$$f_m = m \left(\frac{2n_{\text{eff}}L}{c} - \frac{\theta_r}{\pi f} \right)^{-1} \quad (7)$$

$$Q_m = -\frac{m\pi}{\ln|B|} = \frac{m\pi}{2(\alpha_{\text{eff}}L - \ln|r|)} \quad (8)$$

where m is an integer describing the m th cavity resonance, and θ_r is the phase of reflection coefficient r .

III. CAVITY CHARACTERIZATION

A. Dielectric Samples and Test Fixtures

The materials characterized in this paper were single-crystal substrates polished on both surfaces to an rms roughness tolerance of <1 nm, which were obtained from MTI Corporation. The composition, surface orientation, thickness, and lateral dimensions of the tested substrates are summarized in Table I. Sample thickness was measured at each of the four edges using a microscope, and the mean values are listed. Uncertainty in this measurement was estimated to be ± 2 μm . The surface parallelism derived from thickness measurements was better than 1 mrad.

The dielectric samples were mounted in test fixtures as shown schematically in Fig. 1. Each test fixture had holes to accommodate the alignment pins of the rectangular waveguides forming the cavity. For 10 mm \times 10 mm samples, one corner of the substrate was polished away (by approximately 2 mm) to allow all four alignment pins to pass, while maintaining the orientation shown in Fig. 1. This allowed the anisotropic crystals TiO₂, LiTaO₃, and LiNbO₃ to be mounted such that their extraordinary axis (the c -axis of the crystal) was aligned parallel to either the y -axis or x -axis in Fig. 1, and thus parallel or perpendicular to the y -polarized electric field of the TE_{10} waveguide mode. Fixture thickness was chosen to be approximately 80% that of the substrate, which allowed each sample to be mounted with both surfaces extending beyond those of the test fixture.

In order to form a cavity, a test fixture and sample were mounted as shown in Fig. 1, and light compressive force (approximately 4 N) was applied along the z -axis to ensure contact between the waveguide flanges and the substrate. The data presented correspond to dielectric samples mounted in brass test fixtures. However, tests repeated for SrTiO₃ and TiO₂ using acrylic test fixtures did not produce a significant change in cavity response.

B. Millimeter-Wave Test Procedure

Cavities formed by each dielectric substrate in Table I were measured over four millimeter-wave frequency bands using

a vector network analyzer (VNA) with frequency extension modules. Waveguide dimensions and frequency ranges can be found in [36] (for waveguide widths W_x and W_y satisfying the ratio $W_x = 2W_y$). For each band, a different pair of rectangular waveguides was used to form the waveguide–flange cavities. Measurements were performed at room temperature (20 °C).

Prior to measurements over each frequency band, the VNA response was calibrated. Calibration of W- and G-bands used the TRL method [37] and waveguide calibration standards. For the Ka- and V-bands, a through calibration [37] was used. A dielectric substrate and test fixture were then mounted, compression was applied along the z -axis to form a cavity, and the S-parameters [38] of the cavity were measured. For each measurement, the S-parameters were symmetric ($|S_{uv}| = |S_{vu}|$), indicating good contact between both of the waveguide flanges and the substrate. This allowed S_{21} and S_{11} to be regarded as the transmission and reflection coefficients of the waveguide–flange cavity, respectively.

C. Cavity Response

Fig. 2 shows S_{21} data measured over four frequency bands, for waveguide–flange cavities formed by the same 995- μm -thick SrTiO₃ substrate. The cavities resonated at multiple, uniformly spaced frequencies, and the resonances tended to broaden with increasing frequency. The peak transmission (at resonance) also varied from one frequency band to the next. This trend is in accordance with theoretical calculations of diffractive power loss within the cavity, which are discussed in Section IV.

Fig. 2 also shows results of least-squares fits of measured complex S_{21} data to (1). Individual fits were performed about each resonance peak, over the regions indicated in red, using the fit parameters A , B , and f_m described in Section II. For each fit, r was assumed real positive (an assumption supported by calculations presented in Section IV). As shown, agreement between measured data and the model was quite good. The frequency range of each fit was chosen to minimize the influence of noise far from the resonance frequency.

Although fits to complex S_{11} data were also performed, the additional free parameter r' in the model for S_{11} compared S_{21} caused the fit parameters to be less consistent from resonance to resonance. For this reason, only data based on cavity transmission S_{21} are presented in this paper.

Transmission coefficients of cavities formed by each dielectric substrate in Table I were also measured, and the parameters A , B , and f_m fit for each resonance. However, plots have been omitted for brevity. Agreement between the measured data and the model of (1) was quite good for all the materials and frequencies tested.

D. Effective Refractive Index

In order to determine the effective refractive index of each cavity mode, the resonance number m was first determined by plotting the resonance frequencies for a given substrate as shown in Fig. 3(a). With proper choice of m for each resonance, linear fits of resonance number versus resonance frequency projected to the origin, as shown. The effective

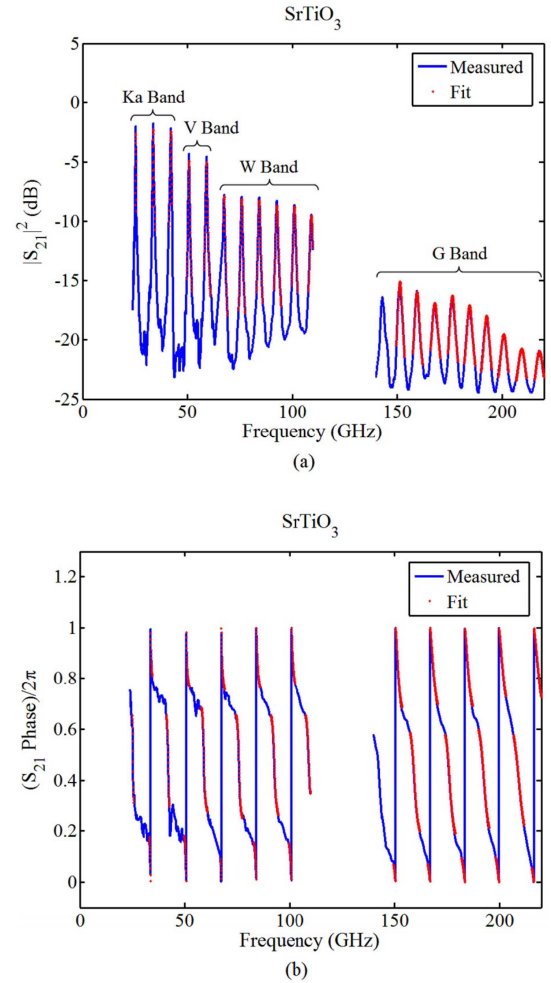


Fig. 2. Transmitted (a) power and (b) phase for a waveguide–flange cavity formed by a 995- μm -thick SrTiO₃ substrate. Measured data (blue), and fits to the measured data about each cavity resonance (red). Data for different frequency bands correspond to cavities formed by the same substrate, but different rectangular waveguides with standard dimensions (see, for instance, [36]).

refractive index of each cavity resonance was then calculated from (7), using the resonance number m and fitted value of the resonance frequency.

Fig. 3(b) shows the effective refractive index versus resonance frequency for waveguide–flange cavities formed by the thickest substrate of each material in Table I. For LiTaO₃, data were similar for both substrate orientations (extraordinary axis \parallel or \perp to the waveguide polarization axis), so data points overlap. In order to clarify these results, Fig. 4 shows the effective relative permittivity, which for nonmagnetic materials can be expressed as

$$\epsilon_{\text{eff}R} = n_{\text{eff}}^2 \quad (9)$$

for the thickest substrate of SrTiO₃ and rutile TiO₂ (\parallel). These plots illustrate the consistency of the measurement technique. Plots for other materials showed similar consistency. For each material, measured values of $\epsilon_{\text{eff}R}$ deviated from the dashed trend line, a least-squares fit to the equation

$$\epsilon_{\text{eff}R} = \epsilon_{\text{eff}R0} + \left(\frac{1}{2} \frac{d^2 \epsilon_{\text{eff}R0}}{df^2} \right) f^2 \quad (10)$$

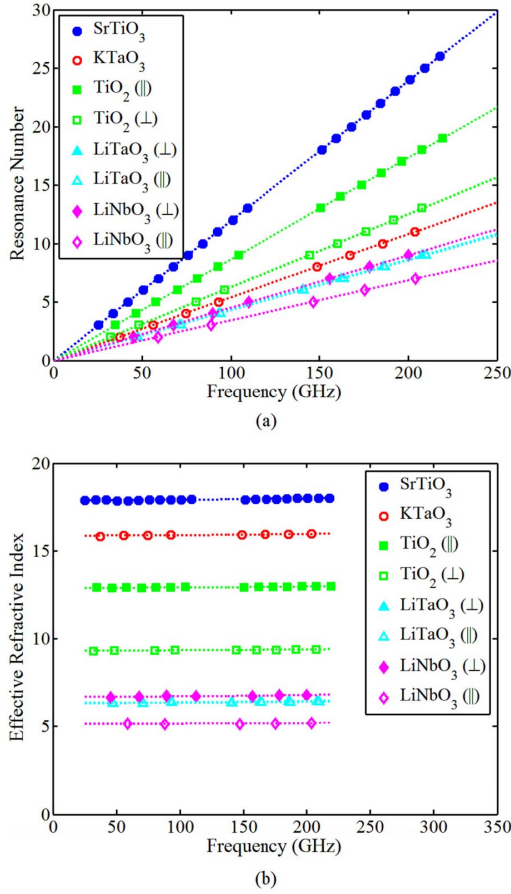


Fig. 3. (a) Resonance number m associated with each measured cavity resonance, chosen such that trend lines extend to the origin. (b) Effective refractive index versus resonance frequency, calculated from fit resonance frequency and (7).

by less than 2%. Such consistency is the result of the same dielectric sample, and the same well-calibrated measurement procedure, being utilized across each frequency band.

Table II lists the values of $\epsilon_{\text{eff}}R_0$ and $\frac{1}{2}d^2\epsilon_{\text{eff}}R_0/df^2$ obtained from least-squares fits to data, for each of the substrates in Table I. Values of $\epsilon_{\text{eff}}R_0$ corresponding to different substrate thicknesses agree to within 0.4%, with the exception of LiTaO₃ (||), for which agreement is within 1.4%. In each case, this variation is consistent with the $\pm 2 \mu\text{m}$ uncertainty in the measured thickness, which translates to relative errors in $\epsilon_{\text{eff}}R_0$ of $\pm 0.8\%$ for substrates 0.5 mm thick, and $\pm 0.4\%$ for substrates 1.0 mm thick, through (7) and (9). Due to greater (relative) accuracy of the thickness measurement, and greater number of data points involved in fits to (10), the fitted values $\epsilon_{\text{eff}}R_0$ and $\frac{1}{2}d^2\epsilon_{\text{eff}}R_0/df^2$ for thicker substrates are more reliable. The number of data points involved in each fit is significant because thinner samples exhibited fewer resonances.

E. Reflection and Propagation Loss

Fig. 5 shows the single-pass power transmission $|r|^2 \exp(-2\alpha_{\text{eff}}L)$ of the resonating cavity mode. Plots for TiO₂ (⊥) and LiNbO₃ have been omitted for brevity. Data are plotted in the form of single-pass power transmission, given in decibels by

$$T_{\text{dB}} = 20 \log_{10} |r|^2 - 2\alpha_{\text{eff}}L \cdot 10 \log_{10} e. \quad (11)$$

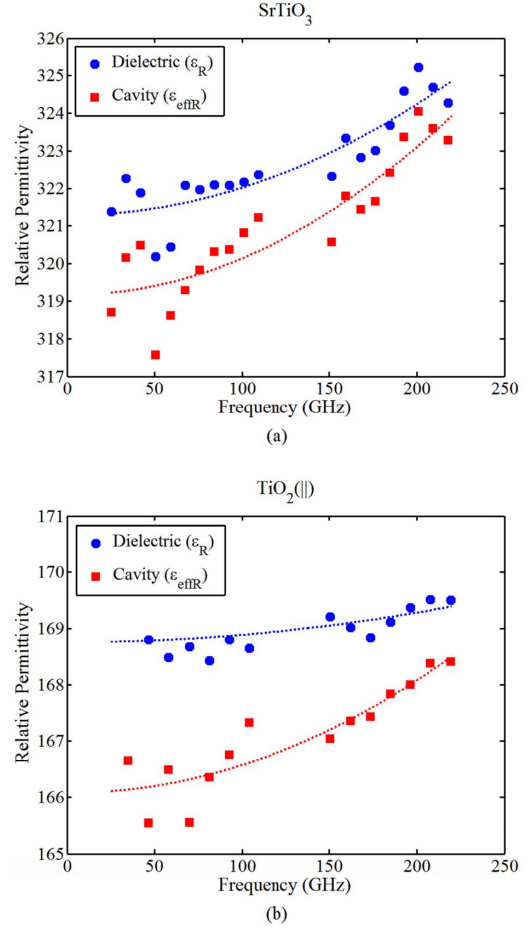


Fig. 4. Effective relative permittivity of the waveguide–flange cavity and relative permittivity of the dielectric substrate versus resonance frequency. For waveguide–flange cavities formed by (a) SrTiO₃ and (b) rutile TiO₂ (||). Trend lines representing the least-squares fits to (10) and (23) are shown as dashed lines.

For SrTiO₃, KTaO₃, and rutile TiO₂ (||), the dashed trend lines in Fig. 5 represent the least-squares fits to the equation

$$T_{\text{dB}} = T_{\text{dB}0} + \left(\frac{1}{2} \frac{d^2 T_{\text{dB}0}}{df^2} \right) f^2. \quad (12)$$

For each of the other materials in Table I, data were instead fit to the equation

$$T_{\text{dB}} = T_{\text{dB}0} + \left(\frac{dT_{\text{dB}0}}{df} \right) f. \quad (13)$$

Although it is apparent that the single-pass power transmission of SrTiO₃, KTaO₃, and rutile TiO₂ (||) cavities were nonlinear with respect to frequency, for other materials the spread of the measured data was too large to distinguish the quadratic contribution to (12), so a linear fit was used instead.

For materials with more than one substrate thicknesses (SrTiO₃, TiO₂, and LiTaO₃), $T_{\text{dB}0}$ was constrained to have the same value for both substrates (for reasons discussed below). This was accomplished by fitting data for each substrate to (12) or (13), and setting $T_{\text{dB}0}$ to the mean value.

In order to distinguish contributions to T_{dB} due to reflection at the substrate–waveguide interface and propagation loss between interfaces (the first and second terms on the right-hand side of (11), respectively), two simplifying

TABLE II
PARAMETERIZED PERMITTIVITY OF CAVITY AND DIELECTRIC

Crystal	Polarization	Thickness (μm)	$\epsilon_{\text{eff}0}$	ϵ_{R0}	$\frac{1}{2}d^2\epsilon_{\text{eff}0}/df^2$ (THz^{-2})	$\frac{1}{2}d^2\epsilon_{R0}/df^2$ (THz^{-2})	$\tan\delta_0$ ($\times 10^{-3}$)	$d\tan\delta_0/df$ ($\text{THz}^{-1} \times 10^{-2}$)
SrTiO ₃	N/A	995	319.2	321.3	98	74	-	6.8
KTaO ₃	N/A	519	239.8	242.1	69	49	-	5.2
Rutile TiO ₂	\parallel c-axis	1001	166.1	169.8	50	13	-	2.5
Rutile TiO ₂	\perp c-axis	1001	86.5	88.2	30	12	≤ 2.1	-
LiTaO ₃	\perp c-axis	1005	40.1	41.9	32	8	≤ 6.9	-
LiTaO ₃	\parallel c-axis	1005	39.9	41.6	23	-0.9	≤ 23	-
LiNbO ₃	\perp c-axis	994	44.5	46.3	36	9	≤ 6.3	-
LiNbO ₃	\parallel c-axis	994	26.3	27.3	10	2.5	-	-
SrTiO ₃	N/A	497	319.6	322.3	92	57	-	6.5
Rutile TiO ₂	\parallel c-axis	484	165.8	169.3	55	16	-	1.9
Rutile TiO ₂	\perp c-axis	484	86.2	88.1	46	25	≤ 6.4	-
LiTaO ₃	\perp c-axis	495	40.7	41.8	14	17	-	-
LiTaO ₃	\parallel c-axis	495	40.1	42.2	17	-16	≤ 13	-

approximations were made. The first approximation was that propagation loss does not contribute significantly to $T_{\text{dB}0}$ when measurement data span multiple frequency bands. This approximation is justified, because as frequency goes to zero, the substrate becomes infinitesimally thin compared to both the wavelength and the waveguide dimensions (which scale with wavelength from band to band), and thus diffractive loss should be negligible in the zero-frequency limit. The other source of propagation loss, dielectric absorption, is generally regarded to be negligible in the zero-frequency limit [38], and thus would also have negligible contribution to $T_{\text{dB}0}$. This first approximation implies that $T_{\text{dB}0}$ must be treated as independent of the cavity length L . Thus, fit values of $T_{\text{dB}0}$ were constrained to have the same value for substrates of different thicknesses, but identical composition and orientation.

The second simplifying approximation was that reflection loss at the substrate-waveguide interface does not contribute significantly to $dT_{\text{dB}0}/df$ or $d^2T_{\text{dB}0}/df^2$ when measurement data span multiple frequency bands. The justification is as follows. It is known that the reflectivity $|r|^2$ at the waveguide-substrate interface depends on both the permittivity and the ratio f/f_c , where f_c is the cutoff frequency of the rectangular waveguide [36]. However, when averaged over the frequency range of each rectangular waveguide band, the average value of f/f_c will be identical for each band. Thus, values of f/f_c at various resonance frequencies will be distributed about the same average value across each frequency band. This implies a distribution of f/f_c across multiple bands that tends to be flat with respect to frequency. The other factor influencing the reflectivity, the permittivity, was approximately independent of frequency for each of the materials tested. Thus, variations in $|r|^2$ due to frequency dependence of the permittivity could also be neglected.

Given the two preceding approximations, theoretical and empirical expressions for single-pass power transmission, (11) and (12) and (13), respectively, combine to yield

$$20\log_{10}|r| \cong T_{\text{dB}0} \quad (14)$$

$$a_{\text{eff}} \cong \left(\frac{da_{\text{eff}0}}{df}\right) f + \left(\frac{1}{2} \frac{d^2a_{\text{eff}0}}{df^2}\right) f^2 \quad (15)$$

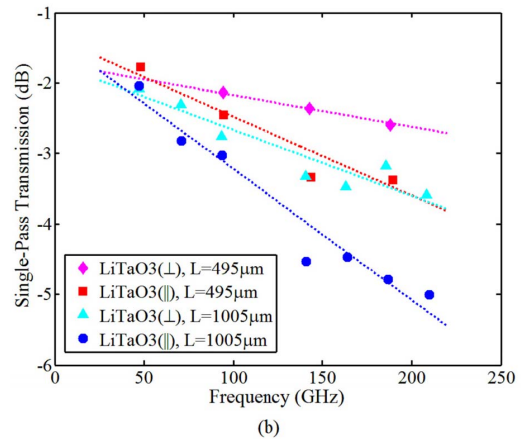
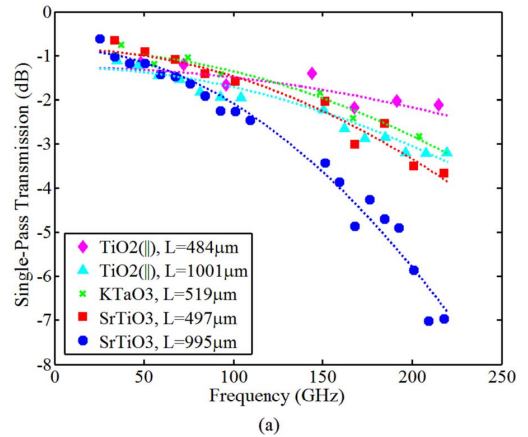


Fig. 5. Cavity single-pass power transmission $|r|^2 \exp(-2a_{\text{eff}}L)$ versus resonance frequency, for cavities formed by various substrates. Determined by fitting measured S_{21} data about each cavity resonance to (1). Trend lines representing the least-squares fits to (a) (12) and (b) (13) are shown as dashed lines.

where

$$\frac{da_{\text{eff}0}}{df} = \left(\frac{-1}{2L\log_{10}e}\right) \frac{dT_{\text{dB}0}}{df} \quad (16)$$

$$\frac{d^2a_{\text{eff}0}}{df^2} = \left(\frac{-1}{2L\log_{10}e}\right) \frac{d^2T_{\text{dB}0}}{df^2} \quad (17)$$

TABLE III
PARAMETERIZED LOSS OF CAVITY AND DIELECTRIC

Crystal	Polarization	Thickness (μm)	$ r ^2_{\text{measured}}$	$ r ^2_{\text{theory}}$	$d\alpha_{\text{eff}}/df$ ($\text{mm}\cdot\text{THz}$) ⁻¹	$d\alpha_0/df$ ($\text{mm}\cdot\text{THz}$) ⁻¹	$\frac{1}{2}d^2\alpha_{\text{eff}}/df^2$ ($\text{mm}\cdot\text{THz}^2$) ⁻¹	$\frac{1}{2}d^2\alpha_0/df^2$ ($\text{mm}\cdot\text{THz}^2$) ⁻¹
SrTiO ₃	N/A	995	0.823	0.845	-	-	14.3	12.8
KTaO ₃	N/A	519	0.818	0.823	-	-	10.8	8.5
Rutile TiO ₂	\parallel c-axis	1001	0.746	0.791	-	-	5.1	3.3
Rutile TiO ₂	\perp c-axis	1001	0.802	0.722	0.99	0.20	-	-
LiTaO ₃	\perp c-axis	1005	0.672	0.619	1.08	0.46	-	-
LiTaO ₃	\parallel c-axis	1005	0.732	0.618	2.13	1.52	-	-
LiNbO ₃	\perp c-axis	994	0.703	0.634	1.15	0.44	-	-
LiNbO ₃	\parallel c-axis	994	0.569	0.551	0.83	0.01	-	-
SrTiO ₃	N/A	497	0.823	0.845	-	-	14.4	12.2
Rutile TiO ₂	\parallel c-axis	484	0.746	0.791	-	-	5.4	2.5
Rutile TiO ₂	\perp c-axis	484	0.802	0.722	1.27	0.63	-	-
LiTaO ₃	\perp c-axis	495	0.672	0.619	1.04	-0.26	-	-
LiTaO ₃	\parallel c-axis	495	0.732	0.618	2.60	0.84	-	-

Table III lists the values of $|r|^2$, $d\alpha_{\text{eff}}/df$ and $\frac{1}{2}d^2\alpha_{\text{eff}}/df^2$ obtained from least-squares fits to data for each of the substrates in Table I. Values of $\frac{1}{2}d^2\alpha_{\text{eff}}/df^2$ corresponding to different substrate thicknesses are consistent for SrTiO₃ and TiO₂ (\parallel). However, for TiO₂ (\perp) and LiTaO₃, values of $d\alpha_{\text{eff}}/df$ vary by as much as 28%. This indicates that loss described by $d\alpha_{\text{eff}}/df$ in Table III is not entirely attributable to the propagation loss within the cavity.

IV. DIELECTRIC CHARACTERIZATION

Having characterized the cavity response, the next step was to compare measurement with theory in order to extract the properties of the dielectric. This analysis was necessary because diffraction within the cavity causes resonant modes to experience propagation loss due to diffraction in addition to dielectric absorption. Diffraction implies that the electromagnetic fields of the cavity mode will have angular spectrum components [40] that propagate off-axis (i.e., not parallel to the z -axis). This also causes the effective refractive index of the cavity mode to differ from the refractive index of the dielectric.

The process of comparing measurement with theory was complicated by the fact that the majority of the tested samples were anisotropic, so models describing radiation from a rectangular waveguide aperture into an isotropic medium [42]–[44] could not be utilized. Thus, theoretical calculations of waveguide–flange cavity response presented in this section are based on calculations performed for that purpose, which are detailed in [44]. By comparing theoretical calculations to measurements of cavity reflectivity, effective refractive index, and propagation loss, the dielectric properties of the substrates forming each cavity could be determined.

For all calculations, the rectangular waveguide was assumed to have widths satisfying the ratio $W_x = 2W_y$, which was consistent with experimental conditions. For simplicity, the metal boundaries of each waveguide and flange were approximated as perfect conductors, and the dielectric and flange were approximated to be infinite in (x, y) . The transverse electric field distributions E_{xu} and E_{yu} at the flange (within the dielectric at $z = \pm L/2$) could then be related to those of the

rectangular waveguide [36] through the relation

$$E_{iu}^{(F)} = \sum_v t_{vu} E_{iv}^{(W)} \cong t_{0u} E_{i0}^{(W)} (i = x, y) \quad (18)$$

where t_{vu} are transmission coefficients, and the superscripts W and F denote waveguide and flange fields, respectively. Calculation of the transverse magnetic field distributions at the flange (H_x and H_y within the dielectric at $z = \pm L/2$) was rather complicated, so is presented in [44]. For all calculations, dielectric absorption was assumed negligible, so calculated propagation loss represented loss due to diffraction, rather than absorption, within the waveguide–flange cavity.

A. Refractive Index and Relative Permittivity

The complex propagation constant of each resonant cavity mode was modeled by the expression

$$\gamma_{uv} = \frac{-1}{L} \ln \left(\frac{P_{uv}^*}{P_u^*} \right) \quad (19)$$

where

$$P_u^* = \frac{1}{2} \iint_{-\infty}^{\infty} (E_{xu}^* H_{yu} - E_{yu}^* H_{xu}) dx dy \quad (20)$$

$$P_{uv}^* = \frac{1}{2} \iint_{-\infty}^{\infty} (E_{xv}^* H_{yu} - E_{yv}^* H_{xu}) dx dy. \quad (21)$$

Here, E_u and H_u are the complex electric and magnetic field distributions of z -propagating flange field u at $z = -L/2$, E_v and H_v are the electric and magnetic field distributions of z -propagating flange field v at $z = L/2$, P_u^* is the complex power flow at $z = -L/2$, and P_{uv}^* is the power coupling (i.e., reaction) from flange field u at $z = -L/2$ to flange field v at $z = L/2$. Calculations of H_{xu} and H_{yu} are discussed in [44]. The theoretical effective refractive index of the cavity mode is related to the complex propagation constant through

$$n_{\text{eff},uv} = \left(\frac{c}{2\pi f_m} \right) \text{Im}(\gamma_{uv}). \quad (22)$$

In order to determine the relative permittivity ϵ_R of the substrate, the permittivity was iterated until the theoretical effective refractive index matched its measured value.

Fig. 4 shows the values of ε_R calculated at each resonance frequency for cavity modes corresponding to the TE₁₀ flange field. Trend lines plotted in Fig. 4 represent the least-squares fits to the expression

$$\varepsilon_R = \varepsilon_{R0} + \left(\frac{1}{2} \frac{d^2 \varepsilon_{R0}}{df^2} \right) f^2. \quad (23)$$

Resulting values of ε_{R0} and $\frac{1}{2}d^2\varepsilon_{R0}/df^2$ are listed in Table II. For each substrate, the difference between the relative permittivity and effective relative permittivity falls within the range $1.0 \leq (\varepsilon_R - \varepsilon_{\text{eff}R}) \leq 3.7$. For different lengths of the same material, values of ε_{R0} are extremely consistent, varying by an average of 0.5%. This variation is consistent with uncertainty in measured thickness, which translates to relative errors in ε_R of $\pm 0.8\%$ for substrates 0.5 mm thick and $\pm 0.4\%$ for substrates 1.0 mm thick. The values of $\frac{1}{2}d^2\varepsilon_{R0}/df^2$ are less consistent, due to the smaller number of data points involved in fits to (10) for thin samples, and relatively low dispersion of the materials. However, for SrTiO₃ and TiO₂(||), values of $\frac{1}{2}d^2\varepsilon_{R0}/df^2$ agree to within 25%. Due to the greater (relative) accuracy of the measured thickness, and greater number of data points involved in fits to (23), fitted values ε_{R0} and $\frac{1}{2}d^2\varepsilon_{R0}/df^2$ are more reliable for thicker substrates.

Equation (23) is consistent with the classical pseudoharmonic model for dielectric response [18], [39] at frequencies far from the dielectric resonance frequency. Relationships between $\frac{1}{2}d^2\varepsilon_{R0}/df^2$ and terms of the classical pseudoharmonic model are provided in the Appendix.

B. Cavity Reflectivity

Reflection coefficients at either end of the waveguide–flange cavity were modeled using the relation [42]

$$r_{uv} = -r'_{vu} = \frac{Y_u^{(W)} - Y_v^{(F)}}{Y_u^{(W)} + Y_v^{(F)}} \quad (24)$$

where $Y_u^{(W)}$ and $Y_u^{(F)}$ are the admittances of various z -propagating waveguide or flange field distributions. The admittances were calculated via [39]

$$Y_u = \frac{2P_u^*}{V_u^2} \quad (25)$$

where P_u^* is the complex power flow in (20) and

$$V_u^2 = \iint_{-\infty}^{\infty} (|E_{xu}|^2 + |E_{yu}|^2) dx dy \quad (26)$$

is the squared voltage. Theoretical values of ε_R from Section IV were assumed when calculating reflection coefficients.

Theoretical values of the reflectivity between TE₁₀ flange field and TE₁₀ waveguide mode are listed in Table III. Reported values represent the average over the operational frequency range $1.24 \leq f/f_c \leq 1.9$ of each rectangular waveguide band [36], where f_c is the cutoff frequency of the waveguide TE₁₀ mode [36], given by

$$f_c = \frac{c}{2W_x} \quad (27)$$

and W_x is the waveguide width.

Calculated reflectivities of other flange field distributions (TE_{*uv*} or TM_{*uv*}) were each equal to 1.00 since the corresponding waveguide modes were below the cutoff. It is apparent from Table III that measured reflectivity most closely matched that of the TE₁₀ flange field distribution. Although there is some discrepancy (the measured reflectivity was on average 0.21 dB higher than predicted, possibly due to measurement error or small contributions from other resonant flange field distributions), these calculations indicate that the resonant cavity mode corresponded to the TE₁₀ flange field distribution at the cavity boundaries ($z = \pm L/2$). For the TE₁₀ flange field distribution, and the range of permittivities tested, the phase of calculated reflection coefficients was between 0.1° and 0.7°. The impact of this on the effective refractive index of the cavity mode would have been negligible, so the phase of the reflection coefficient was approximated as 0°.

C. Diffraction Loss and Absorption

Diffraction loss within the cavity is related to the complex propagation constant through

$$\alpha_{\text{diff},uv} = \text{Re}(\gamma_{uv}). \quad (28)$$

Since theoretical calculations assumed the dielectric substrate to be lossless, theoretical values of the field attenuation coefficient α_{diff} represented attenuation due to diffraction within the cavity. By comparing theoretical values of the diffractive loss to measured values of cavity loss, the field attenuation coefficient α of the dielectric could be estimated via

$$\alpha \cong \alpha_{\text{eff}} - \alpha_{\text{diff}}. \quad (29)$$

Resulting values of single-pass dielectric power loss $\exp(2\alpha L)$ are plotted versus resonance frequency for SrTiO₃, KTaO₃, and rutile TiO₂ (||) in Fig. 6. Plots for other materials have been omitted for brevity.

For SrTiO₃, KTaO₃, and rutile TiO₂ (||), dielectric power loss was fit to the expression

$$\alpha \cong \left(\frac{1}{2} \frac{d^2 \alpha_0}{df^2} \right) f^2. \quad (30)$$

For other materials in Table I, it was instead fit to

$$\alpha \cong \left(\frac{1}{2} \frac{d\alpha_0}{df} \right) f, \quad (31)$$

since loss did not exhibit quadratic frequency dependence. Resulting values of $d\alpha_0/df$ and $\frac{1}{2}d^2\alpha_0/df^2$ are listed in Table III.

Dielectric attenuation coefficients for different thicknesses of SrTiO₃ and TiO₂ (||) in Table III are similar. However, for TiO₂ (⊥) and LiTaO₃, the dielectric attenuation coefficients vary with sample thickness, which indicates that dielectric loss was not fully isolated from other sources of error in the measurement. It follows that values of $d\alpha_0/df$ for TiO₂ (⊥) and LiTaO₃ in Table III are to be treated as the upper bounds on dielectric attenuation. The same can be supposed for LiNbO₃, which had similar levels of attenuation.

By combining (6) with (30) and (31), the dielectric loss tangent can be rewritten as

$$\tan \delta \cong \tan \delta_0 + \left(\frac{d \tan \delta_0}{df} \right) f \quad (32)$$

TABLE IV
DIELECTRIC PROPERTIES AT ROOM TEMPERATURE

Crystal	Polarization	Frequency (GHz)	ϵ_R	$\tan\delta$ ($\times 10^{-3}$)	$\tan\delta/f$ ($\text{THz}^{-1} \times 10^{-2}$)	Method	Reference
SrTiO ₃	N/A	7.2	310	0.4	6	PP	[14]
		3, 6.2, 9.5 / 10	300 / 325	0.4, 0.6, 0.8 / 0.8	13, 10, 9 / 8	DR	[13 / 15]
		10	320	-	-	WG	[16]
		75, 220	310, 290	5, 18	7, 8	QO	[17]
		40-500	360-367	20-30	50-6	TDS	[18]
		25-220	321-325	-	7	WFC	This Work
KTaO ₃	N/A	3, 6, 9 / 10	236 / -	0.14, 0.3, 0.4 / 0.7	5, 5, 5 / 7	DR	[13 / 12]
		10	241	-	-	WG	[16]
		94	229	6	6	WFC	[19]
		25-220	242-244	-	5	WFC	This Work
Rutile TiO ₂	c-axis	4 / 25 / 200	165 / 163 / 164	0.1 / 0.6 / -	2.5 / 2 / -	DR	[20 / 21 / 22]
		22 / 34, 95	170 / 152, 131	- / 0.8, 6.6	- / 2, 7	WG	[23 / 24]
		25-220	170	-	2.5	WFC	This Work
Rutile TiO ₂	⊥ c-axis	4 / 5, 8, 200 / 25	87 / 85, 85, 86 / 86	0.08 / 0.1, 0.2, - / 0.4	2 / 2, 3, - / 1.7	DR	[20 / 21 / 22]
		22 / 34, 94	88 / 80, 82	- / 0.4, 1.8	- / 1.2, 9	WG	[23 / 24]
		25-220	88-89	≤ 2	≤ 8-1	WFC	This Work
LiTaO ₃	⊥ c-axis	1	40	1.3	130	SL	[25]
		94 / 75, 220 / 113	45 / 41, 40 / 44	3 / 3, 8 / 9	3 / 4, 4 / 8	QO	[26 / 17 / 27]
		100-2000	41	-	5.6	TDS	[28]
		25-220	42	≤ 7	≤ 30-3	WFC	This Work
LiTaO ₃	c-axis	1	41	0.7	70	SL	[25]
		94 / 220 / 55, 113	42 / 40 / 30, 49	7 / 14 / 8, 9	7 / 6 / 15, 8	QO	[26 / 17 / 27]
		100-2000	40	-	3.0	TDS	[28]
		25-220	42	≤ 23	≤ 90-10	WFC	This Work
LiNbO ₃	⊥ c-axis	1	44	1.5	150	SL	[25]
		12	42	0.08	0.7	PP	[14]
		94 / 75, 220 / 113	45 / 42, 44 / 46	2 / 8, 8 / 5	2 / 11, 4 / 4	QO	[26 / 17 / 27]
		90-147 / 15-140	43-42 / 44	6.2-6.8 / -	7-5 / -	QO	[29 / 30]
		100-2000	45	-	1.7	TDS	[28]
		25-220	46-47	≤ 6	≤ 25-3	WFC	This Work
LiNbO ₃	c-axis	1	24	1.1	110	SL	[25]
		10	33	0.08	0.8	PP	[14]
		94 / 75, 220 / 55, 113	27 / 28, 26 / 23, 27	2 / 2, 8 / 3, 7	2 / 3, 4 / 5, 6	QO	[26 / 17 / 27]
		90-147 / 15-140	29-28 / 26	7.2-7.8 / -	8-5 / -	QO	[29 / 30]
		100-2000	26	-	1.0	TDS	[28]
		25-220	27	-	-	WFC	This Work

METHODS: SL: SLOTTED LINE DR: DIELECTRIC RESONATOR WFC: WAVEGUIDE-FLANGE CAVITY TDS: TIME DOMAIN SPECTROSCOPY
PP: PARALLEL PLATE WG: WAVEGUIDE QO: QUASI-OPTICAL

where

$$\tan\delta_0 = \left(\frac{c}{\pi\sqrt{\epsilon_R}} \right) \frac{d\alpha_0}{df} \quad (33)$$

$$\frac{d\tan\delta_0}{df} = \left(\frac{c}{2\pi\sqrt{\epsilon_R}} \right) \frac{d^2\alpha_0}{df^2}. \quad (34)$$

The second term in (32) ($d\tan\delta_0/df$) f has the same form as the classical pseudoharmonic model of dielectric response [39], [18], at frequencies far from the dielectric resonance frequency. It represents the intrinsic loss of the dielectric, whereas the first term $\tan\delta_0$ represents the extrinsic loss [5]. The relationship between $d\tan\delta_0/df$ and classical pseudoharmonic model is discussed in the Appendix.

Values of $\tan\delta_0$ and $d\tan\delta_0/df$ are listed in Table II, with values of $\tan\delta_0$ to be regarded as upper bounds on the dielectric loss. Values of $d\tan\delta_0/df$ corresponding to different substrate

thicknesses agree to within 5% for SrTiO₃ and 30% for TiO₂ (||). This level of variation is attributable to measurement error, as is evident from the spread of data in Fig. 6.

V. COMPARISON TO THE LITERATURE

For the purpose of comparison, Table IV lists reported values of ϵ_R and $\tan\delta$ above 1 GHz for each of the materials in Table I. Due to varying levels of uncertainty, ϵ_R has been rounded to a common decimal place, and $\tan\delta$ to a single digit of precision. Table IV also lists the test methods and measurement frequencies. It is clear from Table IV that reported values of ϵ_R vary substantially across the microwave and millimeter-wave frequency range. For LiNbO₃ and LiTaO₃, the majority of reported values are similar, with the exception of significant outliers that vary by as much as 50%. Reported values for rutile TiO₂ are also similar below 30 GHz, but vary by more than 10% in the millimeter-wave region. Values for

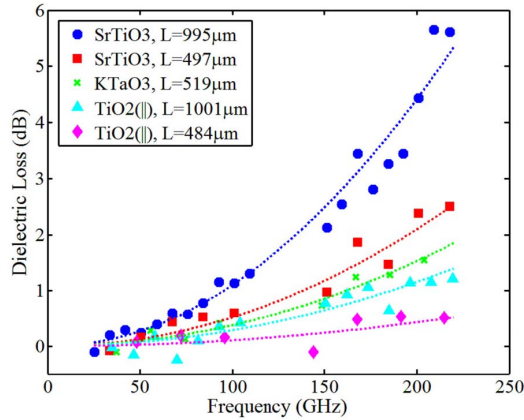


Fig. 6. Single-pass dielectric power loss versus resonance frequency for SrTiO₃, KTaO₃, and rutile TiO₂ (||). Measured data (solid markers) and trend lines (dashed lines) representing the least-squares fits to (31).

KTaO₃ and SrTiO₃ and in Table IV vary by 5% and 25%, respectively.

For both orientations of LiNbO₃ and LiTaO₃, values of ϵ_R in this paper are consistent with the majority of reported ϵ_R values shown in Table IV. Measurements of ϵ_R in Table II are also consistent for samples of different thicknesses. Both results support the validity of relative permittivity measurements in this paper. It follows that they also support the validity of ϵ_R values for other materials in Table II.

Relative permittivities of rutile TiO₂ in Table II are consistent with reported values listed in Table IV other than those from [24]. However, permittivities for rutile TiO₂ in this paper have higher precision across the 25–220-GHz frequency range. Relative permittivities of KTaO₃ and SrTiO₃ in Table II are also reasonably consistent with reported values in Table IV, other than those from [18]. However, permittivities for KTaO₃ and SrTiO₃ reported in work have much higher precision across the 25–220-GHz frequency range.

Loss tangents in Table IV vary widely for each material, so Table IV also lists the values of the ratio $\tan\delta/f$. For time-domain measurements, only this ratio (rather than $\tan\delta$) is provided due to wide frequency ranges involved. According to (32), $\tan\delta/f$ should approach the value $d\tan\delta_0/df$ at sufficiently large frequency. Other than a few relatively large outliers (the lowest frequency values for SrTiO₃, the 95-GHz value for TiO₂, and data from [18]), reported values of $\tan\delta/f$ fall within the range $6\text{--}9 \times 10^{-2} \text{ THz}^{-1}$ for SrTiO₃, $5\text{--}7 \times 10^{-2} \text{ THz}^{-1}$ for KTaO₃, and $2\text{--}3 \times 10^{-2} \text{ THz}^{-1}$ for TiO₂ (||). These are consistent with values of $d\tan\delta_0/df$ measured in this paper, 6.8×10^{-2} , 5.2×10^{-2} , and $2.5 \times 10^{-2} \text{ THz}^{-1}$ for SrTiO₃, KTaO₃, and TiO₂ (||), respectively. Thus, dielectric attenuation values measured for SrTiO₃, KTaO₃, and rutile TiO₂ (||) in this paper can also be regarded as valid data spanning the 25–110 and 140–220 GHz frequency ranges.

VI. CONCLUSION

Using a well-controlled, frequency-scalable measurement procedure based on a waveguide-flange cavity, precise

measurements of the electromagnetic permittivity of five highly refractive, single-crystal materials, SrTiO₃, KTaO₃, rutile TiO₂, LiTaO₃, and LiNbO₃, are presented for frequencies spanning the ranges 25–110 and 140–220 GHz. Real permittivity values are highly consistent for different samples measured across multiple frequency bands. Real permittivities of LiTaO₃ and LiNbO₃ agree with most reported values, supporting the validity of the measurement technique. Notably, the real permittivities measured for SrTiO₃, KTaO₃, and TiO₂ are more consistent with lower frequency values than typically reported in the millimeter-wave region of the spectrum. The intrinsic dielectric loss per unit frequency, measured only for SrTiO₃, KTaO₃ and the extraordinary axis of rutile TiO₂, is consistent with values measured at other frequencies using dielectric resonators and quasi-optical techniques.

APPENDIX

According to the classical pseudoharmonic model of dielectric response [39], [18], complex permittivity can be described as a summation over lattice oscillators. In the single-oscillator model, complex relative permittivity is given by [28]

$$\epsilon_{RC} = \epsilon_{\infty} + (\epsilon_S - \epsilon_{\infty}) \left(\frac{f_0^2}{f_0^2 - f^2 - j\Gamma_0 f} \right) \quad (35)$$

where $(\epsilon_S - \epsilon_{\infty})$, Γ_0 and f_0 represent the strength, width, and frequency of the oscillator, respectively, and ϵ_S is the low frequency limit. At frequencies much less than the oscillator frequency ($f^2 \ll f_0^2$), the relative permittivity and loss tangent can be approximated by

$$\epsilon_R \cong \epsilon_S + \left(\frac{\epsilon_S - \epsilon_{\infty}}{f_0^2} \right) f^2 \quad (36)$$

$$\tan\delta \cong \left[\left(\frac{\epsilon_S}{\epsilon_{\infty}} - 1 \right) \frac{\Gamma_0}{f_0^2} \right] f. \quad (37)$$

Comparison of (36) and (37) with (23) and (32) yields direct relationships between the measured properties ϵ_{R0} , $\sqrt{2}d^2\epsilon_{R0}/df^2$, and $d\tan\delta_0/df$ and properties of the lattice oscillator.

REFERENCES

- [1] R. C. Alferness, "Waveguide electrooptic modulators," *IEEE Trans. Microw. Theory Techn.*, vol. MTT-30, no. 8, pp. 1121–1137, Aug. 1982.
- [2] E. L. Wooten *et al.*, "A review of lithium niobate modulators for fiber-optic communications systems," *IEEE J. Sel. Topics Quantum Electron.*, vol. 6, no. 1, pp. 69–82, Jan./Feb. 2000.
- [3] T. van Duzer, "Superconductor electronics, 1986–1996," *IEEE Trans. Appl. Supercond.*, vol. 7, no. 2, pp. 98–111, Jun. 1997.
- [4] M. J. Lancaster, J. Powell, and A. Porch, "Thin-film ferroelectric microwave devices," *Supercond. Sci. Technol.*, vol. 11, no. 11, pp. 1323–1334, Nov. 1998.
- [5] A. K. Tagantsev, V. O. Sherman, K. F. Astafiev, J. Venkatesh, and N. Setter, "Ferroelectric materials for microwave tunable applications," *J. Electroceram.*, vol. 11, nos. 1–2, pp. 5–66, Sep. 2003.
- [6] N. Klein, A. Scholen, N. Tellmann, C. Zuccaro, and K. W. Urban, "Properties and applications of HTS-shielded dielectric resonators: A state-of-the-art report," *IEEE Trans. Microw. Theory Techn.*, vol. 44, no. 7, pp. 1369–1373, Jul. 1996.

- [7] M. E. Tobar, J. G. Hartnett, E. N. Ivanov, D. Cros, P. Blondy, and P. Guillon, "Cryogenically cooled sapphire-rutile dielectric resonators for ultrahigh-frequency stable oscillators for terrestrial and space applications," *IEEE Trans. Microw. Theory Techn.*, vol. 48, no. 7, pp. 1265–1269, Jul. 2000.
- [8] E. K. Hollmann, O. G. Vendik, A. G. Zaitsev, and B. T. Melekh, "Substrates for high- T_c superconductor microwave integrated circuits," *Supercond. Sci. Technol.*, vol. 7, no. 9, pp. 609–622, Sep. 1994.
- [9] S. J. Fiedziuszko *et al.*, "Dielectric materials, devices, and circuits," *IEEE Trans. Microw. Theory Techn.*, vol. 50, no. 3, pp. 706–720, Mar. 2002.
- [10] G. D. Wilk, R. M. Wallace, and J. M. Anthony, "High- κ gate dielectrics: Current status and materials properties considerations," *J. Appl. Phys.*, vol. 89, no. 10, pp. 5243–5275, May 2001.
- [11] N. Klein, S. Schornstein, I. S. Ghosh, D. Schemion, M. Winter, and C. Zuccaro, "High- Q dielectric resonator devices at cryogenic temperatures," *IEEE Trans. Appl. Supercond.*, vol. 9, no. 2, pp. 3573–3576, Jun. 1999.
- [12] O. G. Vendik, L. T. Ter-Martirosyan, and S. P. Zubko, "Microwave losses in incipient ferroelectrics as functions of the temperature and the biasing field," *J. Appl. Phys.*, vol. 84, no. 2, pp. 993–998, Jul. 1998.
- [13] R. G. Geyer, B. Riddle, J. Krupka, and L. A. Boatner, "Microwave dielectric properties of single-crystal quantum paraelectrics KTaO_3 and SrTiO_3 at cryogenic temperatures," *J. Appl. Phys.*, vol. 97, no. 10, pp. 104111-1–104111-6, May 2005.
- [14] J. Baker-Jarvis, M. D. Janezic, B. Riddle, C. L. Holloway, N. G. Paulter, and J. E. Blendell, "Dielectric and conductor-loss characterization and measurements on electronic packaging materials," NIST, Boulder, CO, USA, Tech. Rep. 1520, Jul. 2001.
- [15] O. G. Vendik, E. K. Hollmann, A. B. Kozyrev, and A. M. Prudan, "Ferroelectric tuning of planar and bulk microwave devices," *J. Supercond.*, vol. 12, no. 2, pp. 325–338, Apr. 1999.
- [16] G. Rupprecht and R. O. Bell, "Dielectric constant in paraelectric perovskites," *Phys. Rev.*, vol. 135, no. 3A, pp. 748–752, Aug. 1964.
- [17] J. S. McCloy, K. A. Korolev, Z. Li, M. N. Afsar, and S. K. Sundaram, "Millimeter-wave dielectric properties of single-crystal ferroelectric and dielectric materials," *IEEE Trans. Ultrason., Ferroelectr., Freq. Control*, vol. 58, no. 1, pp. 18–29, Jan. 2011.
- [18] J. Han, F. Wan, Z. Zhu, and W. Zhang, "Dielectric response of soft mode in ferroelectric SrTiO_3 ," *Appl. Phys. Lett.*, vol. 90, no. 3, pp. 031104-1–031104-3, Jan. 2007.
- [19] D. Rytz, M. B. Klein, B. Bobbs, M. Matlobian, and H. Fetterman, "Dielectric properties of $\text{KTa}_{1-x}\text{Nb}_x\text{O}_3$ at millimeter wavelengths," *Jpn. J. Appl. Phys.*, vol. 24, no. S2, pp. 1010–1012, Jan. 1985.
- [20] M. E. Tobar, J. Krupka, E. N. Ivanov, and R. A. Woode, "Anisotropic complex permittivity measurements of mono-crystalline rutile between 10 and 300 K," *J. Appl. Phys.*, vol. 83, no. 3, pp. 1604–1609, Feb. 1998.
- [21] J. Krupka, K. Derzakowski, G. Annino, M. Cassettari, I. Longo, and M. Martinelli, "Whispering gallery modes in rutile resonators at millimeter wave frequencies," in *Proc. 13th Int. Conf. Microw., Radar Wireless Commun. (MIKON)*, Wroclaw, Poland, vol. 1, May 2000, pp. 41–44.
- [22] N. Klein *et al.*, "Dielectric properties of rutile and its use in high temperature superconducting resonators," *J. Appl. Phys.*, vol. 78, no. 11, pp. 6683–6686, Dec. 1995.
- [23] E. S. Sabisky and H. J. Gerritsen, "Measurements of dielectric constant of rutile (TiO_2) at microwave frequencies between 4.2° and 300°K," *J. Appl. Phys.*, vol. 33, no. 4, pp. 1450–1453, Apr. 1962.
- [24] R. R. Neurgaonkar, L. E. Cross, W. F. Hall, and W. W. Ho, "Research on ferroelectric materials for millimeter wave application," Rockwell Int. Corp., Thousand Oaks, CA, USA, Tech. Rep. AFOSR-TR-83-1299, Aug. 1983.
- [25] J. R. Teague and R. R. Rice, "High frequency dielectric measurements on electro-optic single crystals," *J. Appl. Phys.*, vol. 46, no. 7, pp. 2864–2866, Jul. 1975.
- [26] M. B. Klein, "Phase shifting at 94 GHz using the electro-optic effect in bulk crystals," *Int. J. Infr. Millim. Waves*, vol. 2, no. 2, pp. 239–246, Mar. 1981.
- [27] B. H. Ahn, "Measurement of the indices of refraction and the absorption coefficients of dielectric materials in the millimeter wave region," *J. Appl. Phys.*, vol. 54, no. 4, pp. 2123–2124, Apr. 1983.
- [28] M. Schall, H. Helm, and S. R. Keiding, "Far Infrared properties of electro-optic crystals measured by THz time-domain spectroscopy," *Int. J. Infr. Millim. Waves*, vol. 20, no. 4, pp. 595–604, 1999.
- [29] M. Lee, "Dielectric constant and loss tangent in LiNbO_3 crystals from 90 to 147 GHz," *Appl. Phys. Lett.*, vol. 79, no. 9, pp. 1342–1344, Aug. 2001.
- [30] W. M. Robertson, G. Arjavalingam, and G. V. Kopcsay, "Broadband microwave dielectric properties of lithium niobate," *Electron. Lett.*, vol. 27, no. 2, pp. 175–176, Jan. 1991.
- [31] W. B. Bridges, M. B. Klein, and E. Schweig, "Measurement of the dielectric constant and loss tangent of thallium mixed halide crystals KRS-5 and KRS-6 at 95 GHz," *IEEE Trans. Microw. Theory Techn.*, vol. MTT-30, no. 3, pp. 286–292, Mar. 1982.
- [32] B. Bobbs, M. Matlobian, H. R. Fetterman, R. R. Neurgaonkar, and W. K. Cory, "Electrooptic devices for millimeter waves using cooled ferroelectrics," *Proc. SPIE*, vol. 545, pp. 35–39, Oct. 1985.
- [33] B. Bobbs, M. Matlobian, H. R. Fetterman, R. R. Neurgaonkar, and W. K. Cory, "Millimeter wave absorption and refraction in tungsten bronze ferroelectrics," *Appl. Phys. Lett.*, vol. 48, no. 24, pp. 1642–1644, Jun. 1986.
- [34] J. M. Vaughan, *The Fabry-Perot Interferometer: History, Theory, Practice and Applications*. New York, NY, USA: Taylor & Francis, 1989, pp. 89–92.
- [35] A. Yariv, *Optical Electronics in Modern Communications*, 5th ed. New York, NY, USA: Oxford, 1997, pp. 143–144.
- [36] C. A. Balanis, *Advanced Engineering Electromagnetics*. New York, NY, USA: Wiley, 1989, pp. 353–387.
- [37] J. P. Dunsmore, *Handbook of Microwave Component Measurements: With Advanced VNA Techniques*. London, U.K.: Wiley, 2012, pp. 124–157.
- [38] D. M. Pozar, *Microwave Engineering*, 2nd ed. New York, NY, USA: Wiley, 1998, pp. 196–206.
- [39] A. K. Tagantsev, J. Petzelt, and N. Setter, "Relation between intrinsic microwave and submillimeter losses and permittivity in dielectrics," *Solid State Commun.*, vol. 87, no. 12, pp. 1117–1120, Sep. 1993.
- [40] J. W. Goodman, *Introduction to Fourier Optics*, 2nd ed. New York, NY, USA: McGraw-Hill, 1996, pp. 63–96.
- [41] R. T. Compton, Jr., "The aperture admittance of a rectangular waveguide radiating into a lossy half-space," NASA, Columbus, OH, USA, Tech. Rep. 19640009694, Sep. 1963.
- [42] C. M. Knop and G. I. Cohn, "Radiation from an aperture in a coated plane," *Radio Sci.*, vol. 68D, no. 4, pp. 363–378, Apr. 1964.
- [43] C. A. Balanis, *Antenna Theory: Analysis And Design*, 2nd ed. New York, NY, USA: Wiley 1997, pp. 575–643.
- [44] R. T. Schermer, "Transmission response of a waveguide-flange cavity filled by an anisotropic dielectric," unpublished.

Ross T. Schermer (M'01) received the B.A. degree in physics from the Gustavus Adolphus College, St. Peter, MN, USA, in 1999, and the M.S. and Ph.D. degrees in electrical engineering from the University of Minnesota, Minneapolis, MN, USA, in 2002 and 2004, respectively.

From 2004 to 2007, he was a Post-Doctoral Research Associate with the U.S. Naval Research Laboratory, Washington, DC, USA, supported by a grant from the National Research Council. Since 2007, he has been a Research Physicist with the Optical Sciences Division, U.S. Naval Research Laboratory. He has authored over 25 publications and holds 5 U.S. patents. His current research interests include photonics for communications and sensing, guided-wave electro-optics, and optoelectronic materials.

Dr. Schermer is a member of the Optical Society of America.

Todd H. Stievater is currently a Research Physicist with the Photonics Technology Branch, U.S. Naval Research Laboratory, Washington, DC, USA. His current research interests include nanophotonics, nonlinear optics, semiconductor photonics, cold-atom physics, and photonic integration.

Mr. Stievater is a Senior Member of the Optical Society of America.